CRYSTAL GROWTH & DESIGN

pubs.acs.org/crystal

Article

Stoichiometry-Driven Tuning of Hole Conductivity in MOCVD-Grown β-Ga_2O_3 on *r*-Sapphire Substrates

Zeyu Chi,* Corinne Sartel, Yunlin Zheng, Yves Dumont, and Ekaterine Chikoidze*

Cite This: https://doi.org/10.1021/acs.cgd.5c01728

Read Online

ACCESS | Metrics & More | Article Recommendations

ABSTRACT: β-Ga_2O_3 is a promising ultrawide-band-gap semiconductor for next-generation power and optoelectronic devices, but achieving stable *p*-type conductivity remains a major challenge with the limited understanding of native point defects engineering. In this work, we report a systematic study on the influence of Ga and O flow rates during MOCVD growth on the structural and electrical properties of undoped β-Ga_2O_3 epilayers. Two sets of samples were grown: (i) varying oxygen content to span O/Ga ≈ 180−2700 at a fixed Ga content and (ii) varying gallium content at a fixed O/Ga = 1600. Structural characterization using out-of-plane and in-plane high-resolution X-ray diffraction, Raman spectroscopy, and scanning electron microscopy revealed a strong correlation between growth conditions and film microstructure. Increasing the O/Ga flow ratio improves grain alignment and reduces lattice disorder. Hall effect measurements show the semi-insulating *p*-type conductivity in all samples, with enhancement of native *p*-type conductivity in oxygen-rich conditions, increasing the hole concentration from 6.0×10^{13} to 1.7×10^{15} cm^{-3} at 800 K. Interestingly, the improvement in hole mobility correlates with the increase in Ga content (up to 18.5 $cm^2/V{\cdot}s$) at higher growth rate and improved grain alignment. These results demonstrate that the reproducible control of stoichiometry and microstructure of β-Ga_2O_3 thin films grown by MOCVD provides a possibility to tune native-defect concentrations and thus electrical properties of a material.

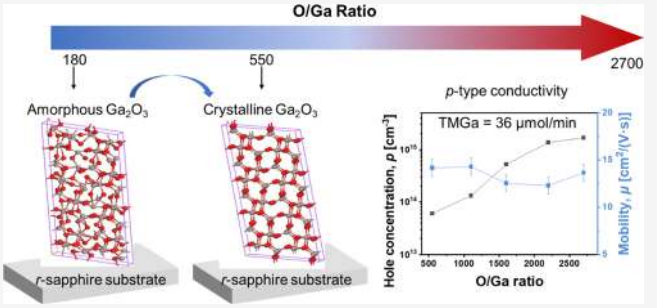

INTRODUCTION

β-Ga_2O_3 exhibits an ultrawide band gap of 4.6−4.9 eV and a predicted high critical electric field larger than 8 MV/cm[1,2]. These properties combined with the commercial availability of 6 in. wafers, controllable *n*-type doping typically in the range of 10^{16}−10^{20} cm^{-3} using elements such as Si,[3,4] Sn,[5,6] Ge[7,8], Nb[9], and Hf,[10] and room-temperature electron mobilities exceeding 200 $cm^2/(V{\cdot}s)$[11]—make it a promising candidate for next-generation power electronics and optoelectronics.[12,13] Its potential has been demonstrated in field-effect transistors,[14,15] Schottky barrier diodes,[16] *p*-NiO/*n*-Ga_2O_3 heterojunction diodes,[17,18] and 2D transistors.[19] Beyond power devices, the large band gap and radiation hardness also make β-Ga_2O_3 attractive for solar-blind UVC photodetectors.[20−22] Excellent radiation tolerance was also reported for different Ga_2O_3 polytypes.[23−25] Despite significant progress in realizing *n*-type doping, achieving reliable *p*-type conductivity remains a critical challenge, which limits the development of bipolar devices (e.g., *p*-*n* junction diodes), while native point defects play a key role in the determination of the electrical properties.

In β-Ga_2O_3, among native defects, oxygen vacancies (V_O's) and gallium vacancies (V_{Ga}'s) are the most studied native defects because their formation is strongly affected by oxygen-rich vs gallium-rich conditions and they critically influence carrier compensation. V_O is predicted to introduce deep levels (>1 eV below the conduction band) and has high formation energy under oxygen-rich conditions.[26−31] Experimentally, V_O has instead been correlated with blue luminescence and is thought to act more as a compensating center than a donor.[32−34] Gallium vacancies (V_{Ga}'s), in contrast, are widely recognized as deep acceptors with lower formation energies under oxygen-rich conditions. EPR,[35] IR,[36] DLTS,[37] and positron annihilation[38] studies demonstrate their role as compensating centers in *n*-type samples. In addition, it was suggested to be the origin of the *p*-type conductivity in semi-insulating samples with an ionization energy of $E_i \sim 1.2$ eV.[37,39,40] In addition to vacancies, oxygen interstitials (O_i's) have also been proposed as relevant native defects under oxygen-rich conditions. First-principles calculations generally predict O_i to introduce deep levels within the band gap, with charge states and stability strongly dependent on the Fermi-level position.[26,31,41] Experimentally, O_i-related defects have

Received: December 9, 2025
Revised: February 26, 2026
Accepted: February 27, 2026

Table 1. Summary of Selected Growth Conditions for β-Ga_2O_3 Films, including TMGa, O_2 Flow Rates, and Growth Duration[a]

sample ID	TMGa (μmol/min)	O_2 (sccm)	O/Ga ratio	duration (min)	thickness (nm)	growth rate (nm/h)	resistivity (Ω·cm)	hole concentration (cm^{-3})	mobility ($cm^2/V·s$)
S1	*36*	100	180	90	860	570			
S2	*36*	110	200	90	1690	1130			
S3	*36*	125	229	90	1850	1230			
S4	*36*	150	270	90	2060	1370			
S5	*36*	200	370	90	2030	1350			
S6	*36*	300	550	90	1890	1260	7.3×10^3	6.0×10^{13}	14.1
S7	*36*	600	1100	90	1805	1200	3.3×10^3	1.2×10^{14}	14.3
S8	*36*	900	1600	90	1850	1230	9.7×10^2	5.1×10^{14}	12.5
S9	*36*	1200	2200	90	1950	1300	3.7×10^2	1.4×10^{15}	12.3
S10	*36*	1500	2700	90	1810	1210	2.7×10^2	1.7×10^{15}	13.6
S11	12	300	*1600*	120	830	415	2.7×10^4	2.4×10^{13}	9.5
S12	24	600	*1600*	105	1450	830	6.3×10^2	9.1×10^{14}	10.9
S13	36	900	*1600*	90	1850	1230	9.7×10^2	5.1×10^{14}	12.5
S14	48	1200	*1600*	75	2050	1640	2.1×10^3	2.2×10^{14}	13.8
S15	60	1500	*1600*	60	2080	2080	5.6×10^2	6.0×10^{14}	18.5

[a]The growth rate and O/Ga ratio were calculated for each sample; the film thickness, hole concentration, and hole mobility were measured for selected samples.

been associated with deep trapping behavior and green luminescence, indicating their potential role in compensation rather than in shallow acceptor doping.[26] Beyond isolated point defects, intrinsic complex defects such as the V_{Ga}–V_O divacancy also contribute to the blue luminescence[32,34,42−45] and may have formation energy comparable to or even lower than isolated vacancies under oxygen-rich conditions; they are charge-active with stability depending on the Fermi level.[29,46] Their acceptor levels are estimated to be from a few hundred millielectrovolts above the valence band to around the midgap. Recent positron annihilation[47] experiments also confirm the presence of such complexes in both conductive and insulating β-Ga_2O_3 samples.

Metal−organic chemical vapor deposition (MOCVD) routinely delivers high-quality epitaxial films with a high growth rate and wafer-scale uniformity. Reported room-temperature mobilities up to 194 $cm^2/(V·s)$[48] and low temperature mobility peaks up to 23,000 $cm^2/(V·s)$[4,49,50] attest to the attainable material quality. This technique is also suitable for controllable *n*-[7,10] and *p*-type doping.[51,52] Critically, the formation and concentration of the point defects mentioned above are strongly dependent on growth conditions such as oxygen partial pressure and cation to anion precursor ratios (O/Ga ratio) during MOCVD growth. Yet, a systematic demonstration that controlling O/Ga stoichiometry can be used to promote native *p*-type conduction remains limited.

Here, we investigate high-temperature *p*-type conductivity in undoped β-Ga_2O_3 epilayers grown under a controlled oxygen/gallium content. By correlating film structural quality X-ray diffraction (XRD) spectra, Raman spectroscopy, and scanning electron microscopy (SEM) images with electrical transport as the O/Ga ratio and the gallium content varied at a fixed O/Ga ratio, we establish specific growth windows that correlate stoichiometry, defect landscape, and microstructural features with the realization of stable, native, semi-insulating *p*-type conduction.

RESULTS AND DISCUSSION

For all of the β-Ga_2O_3 thin films deposited on sapphire substrates, trimethylgallium (TMGa) and O_2 were used as Ga and O sources, respectively. The oxygen-to-gallium molar ratio (O/Ga) was controlled by adjusting the flow of the O_2 and the TMGa vapor pressure. To map how O/Ga stoichiometry governs the growth rate and structural and electrical properties, we prepared two sets of β-Ga_2O_3 samples (S1−S15). Key growth parameters and electrical transport measurement data are summarized in Table 1.

1. First set, fixed TMGa = 36 μmol/min. The O_2 flow was varied from 100 to 1500 sccm, resulting in different O/Ga ratios = 180−2700.

For clarity, samples in this set are referred to by their calculated O/Ga ratios throughout the manuscript; the corresponding sample numbers will also be indicated in each analysis section.

2. Second set, fixed O/Ga ratio = 1600. The O_2 flow was increased from 300 to 1500 sccm in 300 sccm steps, while the gallium supply was proportionally raised from 12 to 60 μmol/min correspondingly in 12 μmol/min steps.

Figure 1a plots the growth rate versus O/Ga ratios at a fixed gallium content. The rate rises with oxygen addition at low O/Ga flux ratio, indicating that oxygen is initially a limiting factor for film growth; beyond O/Ga ratio ≈ 500, the growth rate is invariant, suggesting a transition to gallium-limited growth at this temperature. As shown later, this kinetic crossover coincides with changes in the film morphology and crystalline order. In contrast, Figure 1b shows the growth rate versus Ga content at a fixed O/Ga ratio = 1600. A nearly linear increase

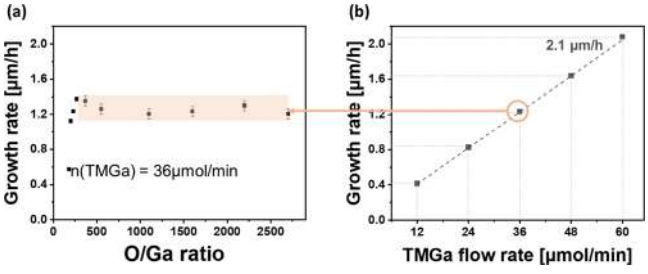

Figure 1. (a) Growth rate vs O/Ga ratios at a fixed gallium content (36 μmol/min). (b) Growth rate versus gallium flow rate at a fixed O/Ga ratio = 1600.

https://doi.org/10.1021/acs.cgd.5c01728
Cryst. Growth Des. XXXX, XXX, XXX−XXX

is observed, consistent with previous reports,[49,53] reaching a maximum growth rate of 2.1 μm/h at 60 μmol/min Ga supply.

Figures 2−4 show detailed XRD analysis of β-Ga_2O_3 films grown at a fixed TMGa content (TMGa = 36 μmol/min), with

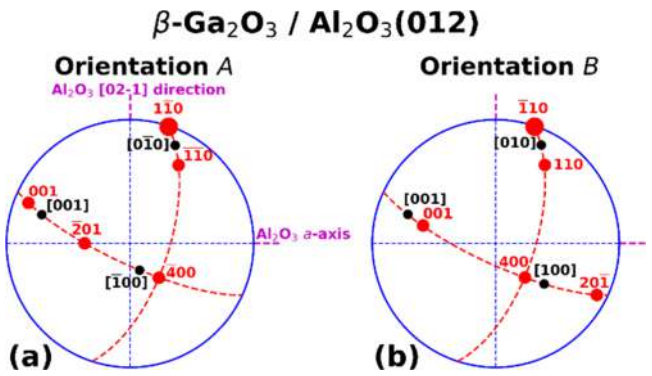

Figure 2. Orientation projections of expected epitaxies of β-Ga_2O_3 on the Al_2O_3 (012) plane: orientation *A* (a) and orientation *B* (b) where the magenta dashed horizontal line indicates the Al_2O_3 *a*-axis azimuth and the vertical one the Al_2O_3 [02−1] direction azimuth. Equivalent orientations *A′* and *B′* are obtained by the substrate vertical *a*-plane mirror symmetry. $\Delta\phi$ used hereafter is defined as the azimuthal angle from the Al_2O_3 [02−1] azimuth. The β-Ga_2O_3 unit-cell axes, namely, the invariant *c* axis ([001]), are indicated by black dots. The red dashed circles outline the sets of HK0 and H0L reflections, which are represented by red dots. β-Ga_2O_3 nearly in-plane 110-type reflections, marked by large red dots, are used for grazing incidence in-plane ϕ-scans to track structural changes in films.

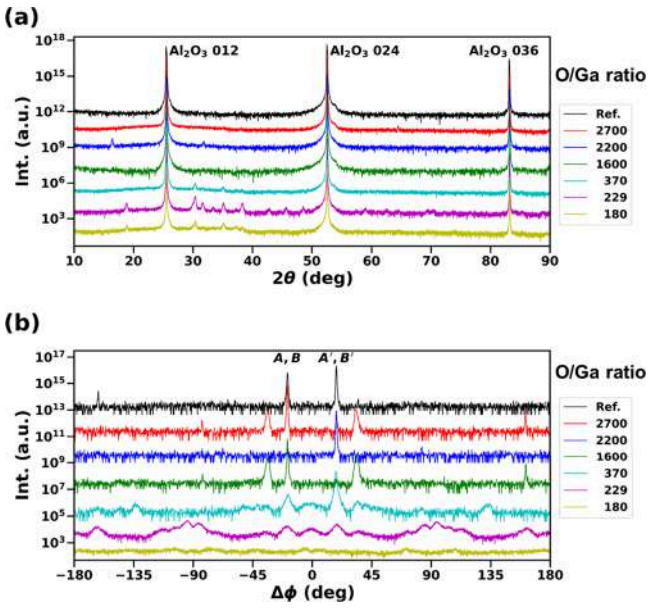

Figure 3. X-ray diffraction of β-Ga_2O_3 films on Al_2O_3 (012) as a function of the O/Ga ratios. (a) $\theta/2\theta$ scans. (b) Grazing incidence in-plane ϕ-scans of β-Ga_2O_3 110-type reflection. The azimuthal angle (−18.3°) of 110 reflections from orientations *A* and *B* is indicated by *A*, *B* and that (+18.3°) from mirror orientations by *A′*, *B′*.

varying O/Ga ratio = 180−2700 (samples S1, S3, S5, S9, and S10). The specific epitaxy of β-Ga_2O_3 on Al_2O_3 (012) differs from conventional epitaxy in that no lattice plane lies in the film plane: no film Bragg peaks are expected on the X-ray $\theta/2\theta$ scan. We showed that the main (−201) lattice planes of β-Ga_2O_3 are tilted relative to the film plane by about 30° toward

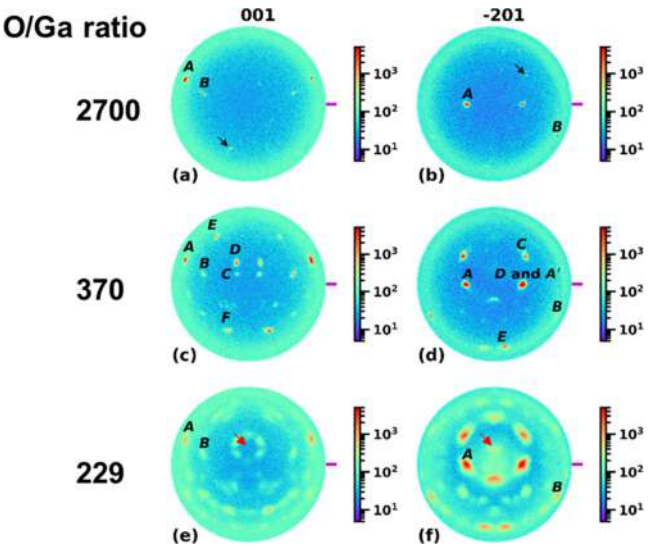

Figure 4. X-ray 001 and −201 pole figures of β-Ga_2O_3 films on Al_2O_3 (012), with O/Ga ratios of 2700, 370, and 229. (a, b) O/Ga ratio = 2700: in addition to spots from orientations *A* and *B* and twinned ones, extra weak spots indicated by black arrows. (c, d) O/Ga ratio = 370: main extra spots labeled by *C*, *D*, *E*, and *F*. (e, f) O/Ga ratio = 229: extra spots organizing into ring structures around an axis, indicated by red arrows, which is tilted by 18° toward the Al_2O_3 [02−1] azimuth.

the *a* axis of Al_2O_3 (Figure 2a).[54,55] This main orientation is called here orientation *A*. A secondary orientation, orientation *B*, was also identified as a twin of *A* in keeping the β-Ga_2O_3 *c* axis (Figure 2b). Two equivalent orientations, *A′* and *B′*, are automatically present due to the symmetry of the substrate *a*-plane mirror. The sample described in ref 54 serves here as a reference to monitor deviations in film orientations as a function of O_2 flow.

At a high O/Ga ratio (≈2700), as expected, only the substrate peaks are present in the X-ray $\theta/2\theta$ scan in Figure 3a, similarly to the references.[54,55] This is inherent to the epitaxy of β-Ga_2O_3 on Al_2O_3 (012), where the main (−201) lattice planes are tilted by ∼30° with respect to the substrate normal, meaning that no film Bragg peaks are expected in a conventional Bragg−Brentano $\theta-2\theta$ geometry. Therefore, the surface orientation and epitaxial relationship of the films are determined by using azimuthal ϕ-scans and pole figure measurements as discussed below. Weak additional peaks appear as the O/Ga ratio decreases from 2700 to 370 and 229, and they become less distinct at O/Ga ratio = 180, where the film approaches a polycrystalline state. However, an increase in background noise level is observed between 20 and 40°, indicating an increase in the overall structural disorder of the film. As sketched in Figure 2, the 110-type reflections associated with orientations *A* and *B* lie nearly in-plane within 1°, or the lattice planes are nearly vertical with respect to the film plane. To further examine the evolution of crystallographic texture, 360° azimuthal ϕ-scans of 110-type reflection are performed (Figure 3b). The peaks associated with orientations *A* and *B*, and symmetrically with orientations *A′* and *B′*, are at azimuths of ±18.3°. Importantly, for all samples where these peaks remain visible, their azimuthal positions stay centered at ±18.3° (within experimental uncertainty), indicating that the epitaxial orientation relationship with the substrate is preserved. The degradation observed at low O/Ga ratios

https://doi.org/10.1021/acs.cgd.5c01728
Cryst. Growth Des. XXXX, XXX, XXX−XXX

actually arises from peak broadening and the emergence of additional orientations, which progressively lead to a quasi-polycrystalline texture, rather than from any modification of lattice parameters. Indeed, the peak widths broaden from 0.4° (O/Ga ratio = 2700 and 2200) to 1.1° (370) and 6.5° (229). Furthermore, broad 110 peaks appear at other unexpected azimuths even with the Ga/O ratio = 2700. The azimuthal modulation of the 110 reflection is clearly visible for the O/Ga ratios = 370 and 229, revealing the existence of multiple grain orientations in these films. For the sample of an O/Ga ratio = 180, the azimuthal modulation nearly vanishes, approaching the case of a polycrystalline ring. These trends indicate a progressive loss of the single-orientation texture with decreasing oxygen content.

To track the multiple film orientations, X-ray pole figures of 001 and −201 reflections were analyzed in the films with O/Ga ratios = 2700, 370, and 229 (Figure 4). At O/Ga ratio = 2700, the 001 and −201 poles are located at the expected tilt and azimuth angles for orientations *A* and *B* and symmetrically for orientations *A*′ and *B*′ (Figure 4a,b). However, the presence of weak peaks reveals a minority orientation (see the arrows in Figure 4a,b). Minority orientations are multiplied at O/Ga ratio = 370, involving at least six orientations labeled *A* to *F* (Figure 4c,d). Here, a couple of 001 and −201 poles are identified as belonging to the same orientation by their relative angle of 49.92°. At O/Ga ratio = 229, the poles are widening in angles (Figure 4e,f). Interestingly, a complex structure, like a ring organization, appears to occur around an axis tilted about 18° toward the Al_2O_3 [0−21] azimuth (see the arrows in Figure 4e,f). It should be noted that for a nearly polycrystalline film such as that with O/Ga ratio = 180, peak broadening would lead to constant intensities in the pole figures, similarly to the 360° ϕ-scans (Figure 3b).

Overall, the $\theta-2\theta$, ϕ-scans, and pole figures clearly demonstrate that films with good structural order are obtained at high O/Ga ratios of 2700 and 2200, with mainly the expected film orientations *A* and *B* and the mirror ones. Meanwhile, lower O/Ga ratios (370 and 229) produce multiple orientations and pronounced angular broadening, indicating increasing structural disorder. Further lowering the O/Ga ratio of 180 results in a nearly polycrystalline film.

Figure 5 shows the Raman spectra recorded in the range of 130−1000 cm^{-1} using 514.5 nm excitation for samples S1, S3, S5, S6, S7, S8, S9, and S10, demonstrating a systematic spectral evolution with O/Ga ratio. As shown in Figure 5a, at lower O/Ga ratios (≤370), spectra exhibit broad, asymmetric peaks with pronounced tailing and elevated background, indicating significant structural disorder and lattice distortions that can be induced by point defect and nonstoichiometry.[56−58] As the O/Ga ratio increases, peaks progressively become sharper and more symmetric, reflecting improved crystallinity of the film and reduced phonon scattering. From an O/Ga ratio of 550, Raman modes can be well-defined. These modes can be classified into three parts: (a) low-frequency modes (100−200 cm^{-1}) attributed to liberations and translations of the Ga_IO_4 tetrahedral and $Ga_{II}O_6$ octahedral chains, (b) midfrequency modes (~310−480 cm^{-1}) corresponding to the deformation of $Ga_{II}O_6$ octahedra, and (c) high-frequency modes (~500−770 cm^{-1}) associated with the stretching and bending of Ga_IO_4 tetrahedral chains.[59,60] In addition to the Ga_2O_3 phonon modes, a broad band in the ~1300−1500 cm^{-1} (not shown in the manuscript) region is observed for samples grown under low O/Ga ratios. This contribution progressively weakens and

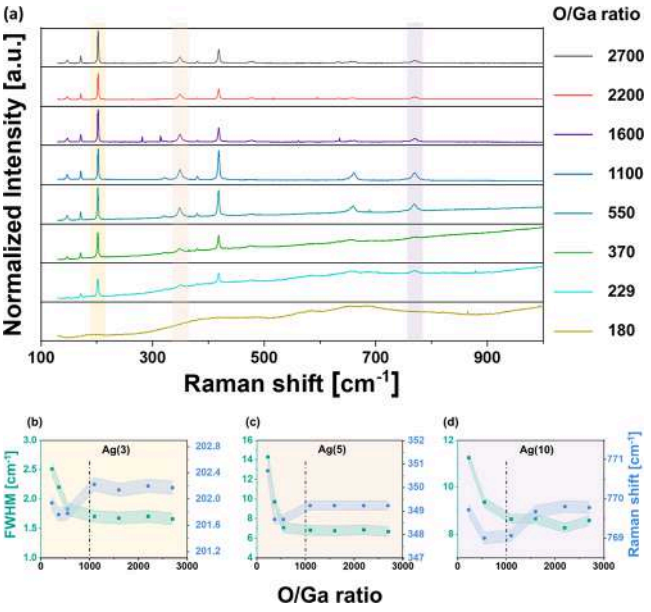

Figure 5. (a) Raman spectra of β-Ga_2O_3 layers with different O/Ga ratios at fixed TMGa = 36 μmol/min. (b−d) Raman shift and fwhm of Ag(3), Ag(5), and Ag(10) modes, respectively.

becomes negligible under an O/Ga ratio = 1100. Such a broad band is commonly attributed to disordered or graphitic carbon and is consistent with residual carbon incorporation originating from the incomplete oxidation of the MO source under oxygen-poor conditions. Although contributions from second-order Ga_2O_3 Raman scattering in this spectral range cannot be fully excluded,[61] the systematic suppression of this band with increasing O/Ga ratio supports its association with carbon-related disorder rather than intrinsic lattice vibrations.

The parameters such as full width at half-maximum (fwhm) and the position of Raman shifts serve as direct probes of lattice dynamics, thermal expansion effect, anharmonic coupling between lattice points, and anharmonic coupling between phonons.[62] To understand the structural evolution in β-Ga_2O_3 layers more clearly, Ag(3), Ag (5), and Ag(10) modes are analyzed as shown in Figure 5b−d. Note that the modes for sample at O/Ga ratio = 180 and the mode Ag(10) for sample O/Ga ratio = 370 are not available due to insufficient definition. All three modes show clear narrowing of fwhm with different levels from low to intermediate O/Ga ratio, reflecting improved lattice order. At higher O/Ga ratios (>1100), the variations of both Raman shift and fwhm plateau, reaching a regime where further changes drop below the spectral resolution limit (~0.2 cm^{-1}) in our system, indicating that the crystallinity improvement is less significant with further increase in oxygen flow during the growth. In particular, the Ag(5) mode exhibits the most pronounced narrowing of fwhm from 14.3 to 6.7 cm^{-1} (Figure 5c), highlighting its exceptional sensitivity. Similar observations were reported in refs 62 and 63 for β-Ga_2O_3 single crystals. The Ag(5) Raman mode was identified as the most sensitive to uniaxial stress along the ⟨010⟩ direction, exhibiting the largest sharpening under deformation, making it well suited for evaluating internal stress and lattice strain in β-Ga_2O_3, which further confirms that oxygen-rich growth conditions relieve structural stress and improve crystalline order. Besides, the pronounced intensity of the Ag(3) mode can be attributed to its exceptionally large Raman tensor elements among the Raman-active Ag modes,[64]

https://doi.org/10.1021/acs.cgd.5c01728
Cryst. Growth Des. XXXX, XXX, XXX−XXX

which induce a strong modulation of the crystal polarizability and thus a markedly enhanced Raman scattering cross section. There is less discussion on the Ag10 mode that originates from high-frequency GaO_4 stretching vibrations; it is therefore sensitive to local stoichiometry and tetrahedral-unit strain, making its redshift and narrower, a clear indicator of reduced disorder under oxygen-rich growth.

To probe how the microstructure evolves with the O/Ga ratio and with Ga content at a fixed O/Ga ratio, scanning electron microscope (SEM) analysis was carried out (Figure 6). All cross-section SEMs were taken from samples cleaved along the same substrate azimuth and imaged under identical conditions.

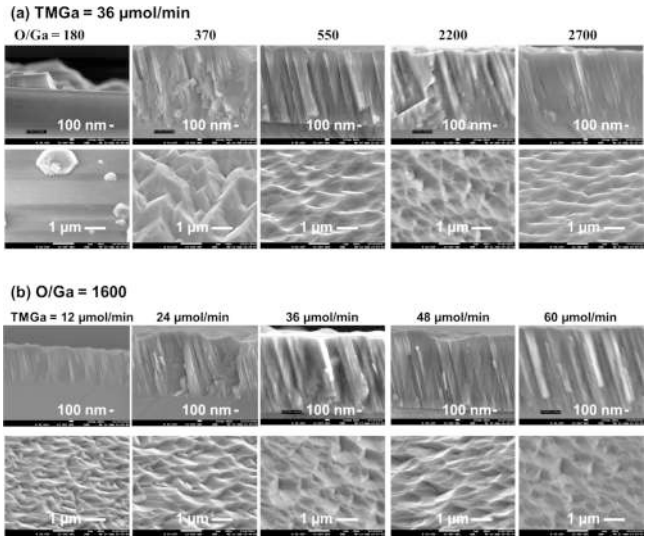

Figure 6. SEM cross-sectional and top-view images of β-Ga_2O_3 films grown at (a) TMGa = 36 μmol/min with varying O/Ga ratios = 180−2700 and (b) O/Ga ratio = 1600 with TMGa = 12−60 μmol/min.

At a constant Ga content (TMGa = 36 μmol/min) with varying O/Ga ratios (samples S1, S5, S6, S9, and S10), the SEM cross-sectional and surface images (Figure 6a) demonstrate a clear structural evolution as the O_2 flow increases. Under O/Ga ratios <370, the films exhibit pronounced faceting, coarse surface morphology, and randomly oriented and short columns in the cross section. Increasing the O/Ga ratio to ∼1100 produces a marked transition to dense, better coalesced surfaces and more aligned columnar grains that run through the thickness. A further increase to 2200−2700 does not significantly alter the microstructure. These observations are consistent with the XRD results, which reveal the transition from polycrystalline to single-orientation films with larger and larger coherence lengths as the level of the O_2 flow increases. In addition, the azimuthal broadening of the in-plane XRD reflections decreases in the same trend, highlighting a reduction in structural disorder and misorientation.

At a fixed O/Ga ratio = 1600, the influence of increasing TMGa molar flow on film morphology is shown in Figure 6b for samples S11, S12, S13, S14, and S15. Top-view SEM images show that the surface evolves from rough and granular at low TMGa (12−24 μmol/min) to smoother and more uniform at higher TMGa values (48−60 μmol/min), reflecting improved surface coverage and grain coalescence. Cross-sectional SEM images further reveal longer and more parallel columns along the growth direction with increasing TMGa, indicating enhanced vertical crystallinity and a preferred orientation. These changes reflect a transition from sparse, short grains to dense and well-aligned microstructures, which may play a crucial role in enhancing charge carrier transport.

The well-crystallized samples (O/Ga ratios ≥ 550) were selected for electrical transport measurements, carried out at 800 K as the samples are semi-insulating as room temperature. The ohmic contacts were prepared by the silver paste at four corners of each square-shaped sample of 1 × 1 cm and measured in a Van der Pauw configuration.

Here, the $I-V$ characteristic and the Hall voltage (V_H) versus the applied magnetic field (B) at 800 K of sample S10 (with the fastest growth rate (2.08 μm/h)) in this series are shown as an example (Figure 7). The $I-V$ curve shows a linear response, ensuring the subsequent electrical transport measurement. The Hall voltage increases linearly with the applied magnetic field from −1.6 to +1.6 T, confirming p-type conduction. All of the other studied samples exhibit similar behavior and thus exhibit a p-type nature. Such semi-insulating p-type conductivity has been discussed in the context of an established defect framework, where V_{Ga}-related defects have been widely reported to act as dominant acceptors in p-type β-Ga_2O_3 or compensating centers in n-type β-Ga_2O_3.[37−39]

Figure 8a,b shows the electrical transport behavior with increasing O/Ga ratios at a fixed Ga content (TMGa = 36 μmol/min) (samples S6, S7, S8, S9, and S10). Resistivity (ρ) continuously decreases from 7.3×10^3 to 2.7×10^2 Ω·cm with increasing O/Ga ratios from 550 to 2700. At relatively low O/Ga ratios (<1600), increasing the O/Ga ratio leads to a more

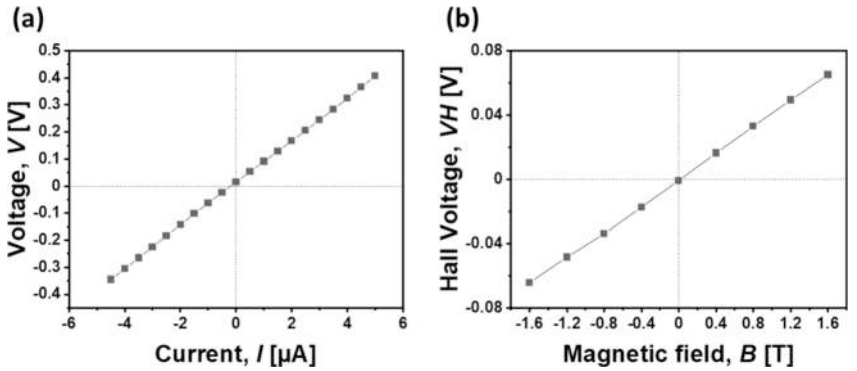

Figure 7. (a) $I-V$ characteristic. (b) Hall voltage as a function of perpendicularly applied magnetic field from −1.6 to 1.6 T at 800 K for sample S10.

https://doi.org/10.1021/acs.cgd.5c01728
Cryst. Growth Des. XXXX, XXX, XXX−XXX

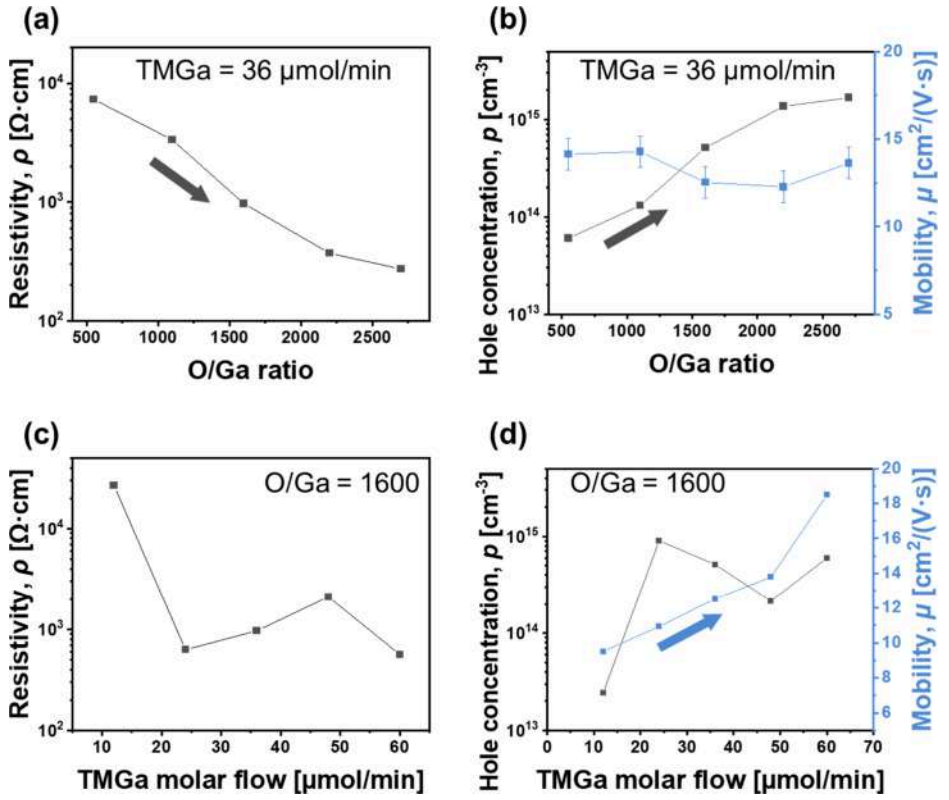

Figure 8. Electrical measurement at 800 K for semi-insulating β-Ga_2O_3 films. (a, b) Samples grown at fixed TMGa = 36 μmol/min: resistivity, hole concentration, and mobility vs O/Ga ratio. (c, d) Samples grown at fixed O/Ga ratio = 1600: resistivity, hole concentration, and mobility vs TMGa flow rates. Arrows indicate the general evolution trend of the electrical transport parameters with increasing O/Ga ratio or Ga content.

pronounced decrease in resistivity. This suggests a progressive modification of film stoichiometry and a reduction of donor-like compensating defects commonly associated with oxygen-deficient growth conditions. Beyond O/Ga ratio ≈ 2200, further oxygen addition during the growth results in less significant resistivity change, indicating that the electrical behavior cannot be explained solely by the suppression or filling of oxygen vacancies. Instead, additional defect-related mechanisms are expected to contribute to the observed transport behavior. In particular, complex defects such as V_{Ga}−V_O divacancies were predicted to have comparable or even lower formation energy than single vacancies in oxygen-rich conditions based on *ab initio* and DFT calculations,[29,46] indicating their potential stability during oxygen-rich condition growth. They are also believed to be responsible for the appearance of a shallow acceptor center in the oxygen annealed β-Ga_2O_3 sample[65] and layers grown under high O/Ga ratio.[54] Nevertheless, their role in the present study should be regarded as consistent with the observed trends rather than as a definitive attribution. In addition, oxygen interstitials (O_i), which are thermodynamically favored under oxygen-rich conditions, may also influence the electrical transport behavior.[26,31,41] The enhancement of the *p*-type conductivity can be mainly attributed to the increase of hole concentration as shown in the Figure 8b from 6.0×10^{13} to 1.7×10^{15} cm^{-3} in the O/Ga ratio range of 550 to 2700. Meanwhile, the Hall mobility was determined to be in the range of 12.3 and 14.3 $cm^2/(V{\cdot}s)$ without a clear dependence on the O_2 flow. This trend corresponds to the observations in SEM and XRD in-plane scans showing that a further increase in the flow of the O_2 does not significantly improve the crystalline quality.

Figure 8c,d shows the electrical transport behavior when O/Ga ratio was fixed at 1600 (samples S11, S12, S13, S14, and S15). Resistivity drops at relatively lower Ga supply (12−24 μmol/min), from 2.7×10^4 to 6.3×10^2 Ω·cm, and becomes relatively stable above (Figure 8c), which can be mainly attributed to the increase of hole concentration. Notably, the hole mobility continuously increases from 9.5 to 18.5 $cm^2/(V{\cdot}s)$ with higher Ga content during film growth. This observation may correlate with the evolution of film morphology observed by SEM; increasing Ga content leads to elongated and more uniformly aligned columnar structures. Such microstructural evolution is expected to improve effective charge transport pathways and reduce carrier scattering, thereby enhancing mobility, although nanoscale defect structures such as intragrain defects and nanoscale grain boundaries cannot be directly resolved by SEM.

In summary, these results demonstrate that the electrical transport properties of undoped semi-insulating *p*-type β-Ga_2O_3 films can be effectively tuned. The O/Ga ratio primarily sets the free carrier density through defect chemistry, whereas the gallium content (at fixed O/Ga) influences film texture and microstructural alignment, leading to enhanced free hole mobility.

The vapor pressure of TMGa was determined by the bubbler temperature (set to −14 °C in this work). Under these conditions, the TMGa molar flow was tuned from 12 to 60 μmol/min, while the O_2 flow rate was set from 100 to 1500 sccm, resulting in O/Ga molar ratios ranging from ∼200 to ∼2700, as summarized in Table 1.

https://doi.org/10.1021/acs.cgd.5c01728
Cryst. Growth Des. XXXX, XXX, XXX−XXX

CONCLUSIONS

This work demonstrates that the structural and electrical properties of undoped β-Ga_2O_3 epilayers can be effectively tuned by controlling the O/Ga stoichiometry during MOCVD growth. By systematically varying the O/Ga ratio and TMGa molar flow, we identify key growth parameters when the films exhibit enhanced crystallinity and semi-insulating (high-temperature) *p*-type conductivity. By varying the O/Ga ratio (≈180−2700) at a fixed Ga content (TMGa = 36 μmol/min), we identify an oxygen-rich condition range where texture alignment improves, lattice disorder decreases, and well-oriented columnar grains emerge. XRD and Raman spectra evidence a transition from polycrystalline to aligned textures with increasing oxygen flow, while electrical resistivity reduction is primarily driven by an increase in free hole concentration. In contrast, varying the gallium content (TMGa = 12−60 μmol/min) at a fixed O/Ga ratio = 1600 refines the microstructure, promoting vertical grain elongation, with a corresponding enhancement of hole mobility from 9.5 to 18.5 $cm^2/V{\cdot}s$ with comparable carrier densities. Overall, our results show that adjusting the oxygen/gallium flow during the deposition, i.e., varying stoichiometry, systematically can tune electrical transport properties of semi-insulating *p*-type β-Ga_2O_3 thin films. We believe that the present work establishes a growth technology capable of manipulating native point defects, thereby enabling both a fundamental understanding and practical realization of hole conductivity in β-Ga_2O_3.

EXPERIMENTAL DETAILS

Thin Film Growth

All Ga_2O_3 samples were grown in an RF-heated horizontal MOCVD reactor on Al_2O_3 (012) (*r*-oriented sapphire) substrates. A standard substrate cleaning procedure was applied prior to growth. The substrates were sequentially cleaned in acetone, isopropanol, and deionized water in an ultrasonic bath, 15 min each, followed by drying under a N_2 flow. Trimethylgallium (TMGa) and O_2 were used as precursors for Ga and O, respectively, with separated inlets between TMGa and O_2 to avoid premature reactions in the manifold. The growth was carried out under quasi-hot-wall conditions: in addition to the heated substrate holder, the surrounding chamber walls in quartz were also heated to keep the temperature. The temperature and pressure in the growth chamber were kept at 825 °C and 33 Torr, respectively. The TMGa bubbler temperatures were fixed at −14 °C. Key growth parameters and measurement results for both sets are summarized in Table 1.

Raman Spectra

Raman spectra were recorded by using a Renishaw inVia Reflex micro-Raman spectrometer at room temperature. The samples were excited using a cw Modu-Laser Stellar-RMN laser emitting at 514.5 nm with a power of 2−4 mW. The reflecting microscope objective was 50 with NA 0.75; the excitation spot diameter was 1 mm. The backscattered light was dispersed by a monochromator with a spectral resolution of 1.4 cm^{-1}. The light was detected by a charge coupled device. The typical accumulation time was 30 s. Raman shifts were calibrated using an optical phonon frequency (520.5 cm^{-1}) of a silicon nanocrystal.

Scanning Electron Microscopy

Surface morphologies of films were obtained by FEG SEM 7001-F JEOL. The electron source was produced by a field effect cannon. The Everhart−Thornley electron secondary detector had a resolution of 1.2 nm at 30 kV and 1 nm at 1 kV. The acceleration voltage and beam current were varied from 1 to 30 kV and 1 pA to 200 nA, respectively. Image magnification was up to 1,000,000×.

X-ray Diffraction

The structure of the samples was studied using X-ray diffraction (XRD). Data were collected on a five-circle diffractometer (Rigaku SmartLab) with Cu Kα radiation from a rotating anode (40 kV, 9 kW). For out-of-plane (OP) measurements, Cu Kα1 radiation was selected by a channel-cut Ge(220) two-reflection monochromator. The film in-plane (IP) orientation and strain were probed by grazing incidence XRD (GIXRD) at a constant incidence of 0.5° without a monochromator. The film global orientation texture was explored by X-ray pole figures (PFs) using the IP PF configuration.

Hall Effect Measurements

Ohmic contacts were prepared by silver paint at the four corners of the sample. Hall effect measurements were performed by a home-built high-impedance, high-temperature setup in a Van der Pauw configuration at 800 K applying the magnetic fields perpendicularly to the film plane varying from −1.6 to 1.6 T under a N_2 environment.

AUTHOR INFORMATION

Corresponding Authors

Zeyu Chi − *Groupe d'Etude de la Matière Condensée (GEMaC), Université Paris-Saclay, UVSQ-CNRS, Versailles 78035, France;* orcid.org/0000-0003-1391-527X; Email: zeyu.chi@uvsq.fr

Ekaterine Chikoidze − *Groupe d'Etude de la Matière Condensée (GEMaC), Université Paris-Saclay, UVSQ-CNRS, Versailles 78035, France;* orcid.org/0000-0002-6566-4639; Email: ekaterine.chikoidze@uvsq.fr

Authors

Corinne Sartel − *Groupe d'Etude de la Matière Condensée (GEMaC), Université Paris-Saclay, UVSQ-CNRS, Versailles 78035, France*

Yunlin Zheng − *Institut des Nano Sciences de Paris (INSP), CNRS UMR7588, Sorbonne Université, Paris 75252, France*

Yves Dumont − *Groupe d'Etude de la Matière Condensée (GEMaC), Université Paris-Saclay, UVSQ-CNRS, Versailles 78035, France;* orcid.org/0000-0002-0739-428X

Complete contact information is available at: https://pubs.acs.org/10.1021/acs.cgd.5c01728

Notes

The authors declare no competing financial interest.

ACKNOWLEDGMENTS

This work has been funded by "GALLIA" International Research Project (CNRS, France), French National Agency of Research (ANR), project "GOPOWER", CE-50 N0015-01, and MRSEI PHC-Maimonide N50047TD.

REFERENCES

(1) Higashiwaki, M.; Sasaki, K.; Kuramata, A.; Masui, T.; Yamakoshi, S. Gallium Oxide (Ga2O3) Metal-Semiconductor Field-Effect Transistors on Single-Crystal β-Ga2O3 (010) Substrates. *Appl. Phys. Lett.* **2012**, *100* (1), No. 013504.

(2) Chikoidze, E.; Tchelidze, T.; Sartel, C.; Chi, Z.; Kabouche, R.; Madaci, I.; Rubio, C.; Mohamed, H.; Sallet, V.; Medjdoub, F.; Perez-Tomas, A.; Dumont, Y. Ultra-High Critical Electric Field of 13.2 MV/Cm for Zn-Doped p-Type β-Ga2O3. *Mater. Today Phys.* **2020**, *15*, No. 100263.

(3) Goto, K.; Konishi, K.; Murakami, H.; Kumagai, Y.; Monemar, B.; Higashiwaki, M.; Kuramata, A.; Yamakoshi, S. Halide Vapor Phase Epitaxy of Si Doped β-Ga_2O_3 and Its Electrical Properties. *Thin Solid Films* **2018**, *666*, 182−184.

https://doi.org/10.1021/acs.cgd.5c01728
Cryst. Growth Des. XXXX, XXX, XXX−XXX

(4) Feng, Z.; Anhar Uddin Bhuiyan, A. F. M.; Karim, M. R.; Zhao, H. MOCVD Homoepitaxy of Si-Doped (010) β-Ga_2O_3 Thin Films with Superior Transport Properties. *Appl. Phys. Lett.* **2019**, *114* (25), No. 250601.
(5) Mauze, A.; Zhang, Y.; Itoh, T.; Wu, F.; Speck, J. S. Metal Oxide Catalyzed Epitaxy (MOCATAXY) of β-Ga2O3 Films in Various Orientations Grown by Plasma-Assisted Molecular Beam Epitaxy. *APL Mater.* **2020**, *8* (2), No. 021104.
(6) Kuang, S.; Yang, Z.; Zhang, Z.; Sheng, Z.; Wei, S.; Chen, Y.; Xu, W.; Yang, Y.; Chen, D.; Qi, H.; Zhang, K. H. L. Transport and Electronic Structure Properties of MBE Grown Sn Doped Ga2O3 Homo-Epitaxial Films. *Mater. Today Phys.* **2024**, *48*, No. 101555.
(7) Alema, F.; Seryogin, G.; Osinsky, A.; Osinsky, A. Ge Doping of β-Ga2O3 by MOCVD. *APL Mater.* **2021**, *9* (9), No. 091102.
(8) Ranga, P.; Bhattacharyya, A.; Whittaker-Brooks, L.; Scarpulla, M. A.; Krishnamoorthy, S. N-Type Doping of Low-Pressure Chemical Vapor Deposition Grown β-Ga2O3 Thin Films Using Solid-Source Germanium. *J. Vac. Sci. Technol. A* **2021**, *39* (3), No. 030404.
(9) Zhou, W.; Xia, C.; Sai, Q.; Zhang, H. Controlling N-Type Conductivity of β-Ga2O3 by Nb Doping. *Appl. Phys. Lett.* **2017**, *111* (24), No. 242103.
(10) Saleh, M.; Varley, J. B.; Jesenovec, J.; Bhattacharyya, A.; Krishnamoorthy, S.; Swain, S.; Lynn, K. Degenerate Doping in β-Ga2O3 Single Crystals through Hf-Doping. *Semicond. Sci. Technol.* **2020**, *35* (4), No. 04LT01.
(11) Rajapitamahuni, A. K.; Manjeshwar, A. K.; Kumar, A.; Datta, A.; Ranga, P.; Thoutam, L. R.; Krishnamoorthy, S.; Singisetti, U.; Jalan, B. Plasmon−Phonon Coupling in Electrostatically Gated β-Ga2O3 Films with Mobility Exceeding 200 Cm2 V−1 s−1. *ACS Nano* **2022**, *16* (6), 8812−8819.
(12) Liu, Z.; Tang, W. A Review of Ga2O3 Deep-Ultraviolet Metal−Semiconductor Schottky Photodiodes. *J. Phys. Appl. Phys.* **2023**, *56* (9), No. 093002.
(13) Pearton, S. J.; Ren, F.; Polyakov, A. Y.; Haque, A.; Labed, M.; Rim, Y. S. Status of Ga2O3 for Power Device and UV Photodetector Applications. *Appl. Phys. Rev.* **2025**, *12* (3), No. 031336.
(14) Higashiwaki, M.; Sasaki, K.; Kamimura, T.; Hoi Wong, M.; Krishnamurthy, D.; Kuramata, A.; Masui, T.; Yamakoshi, S. Depletion-Mode Ga2O3Metal-Oxide-Semiconductor Field-Effect Transistors on β-Ga2O3 (010) Substrates and Temperature Dependence of Their Device Characteristics. *Appl. Phys. Lett.* **2013**, *103* (12), No. 123511.
(15) Lu, C.-H.; Tarntair, F.-G.; Kao, Y.-C.; Tumilty, N.; Horng, R.-H. Undoped β-Ga2O3 Layer Thickness Effect on the Performance of MOSFETs Grown on a Sapphire Substrate. *ACS Appl. Electron. Mater.* **2024**, *6* (1), 568−575.
(16) Li, W.; Saraswat, D.; Long, Y.; Nomoto, K.; Jena, D.; Xing, H. G. Near-Ideal Reverse Leakage Current and Practical Maximum Electric Field in β-Ga2O3 Schottky Barrier Diodes. *Appl. Phys. Lett.* **2020**, *116* (19), No. 192101.
(17) Zhang, J.; Dong, P.; Dang, K.; Zhang, Y.; Yan, Q.; Xiang, H.; Su, J.; Liu, Z.; Si, M.; Gao, J.; Kong, M.; Zhou, H.; Hao, Y. Ultra-Wide Bandgap Semiconductor Ga2O3 Power Diodes. *Nat. Commun.* **2022**, *13* (1), 3900.
(18) Zhou, F.; Gong, H.; Xiao, M.; Ma, Y.; Wang, Z.; Yu, X.; Li, L.; Fu, L.; Tan, H. H.; Yang, Y.; Ren, F.-F.; Gu, S.; Zheng, Y.; Lu, H.; Zhang, R.; Zhang, Y.; Ye, J. An Avalanche-and-Surge Robust Ultrawide-Bandgap Heterojunction for Power Electronics. *Nat. Commun.* **2023**, *14* (1), 4459.
(19) Nguyen, T. D.; Tu, Q.; Zhang, X.; Lin, Y. C. A Printed Gallium Oxide Dielectric for 2D Transistors. *Nat. Electron.* **2024**, *7* (12), 1078−1079.
(20) Flack, T. J.; Pushpakaran, B. N.; Bayne, S. B. GaN Technology for Power Electronic Applications: A Review. *J. Electron. Mater.* **2016**, *45* (6), 2673−2682.
(21) Kalra, A.; Muazzam, U. U.; Muralidharan, R.; Raghavan, S.; Nath, D. N. The Road Ahead for Ultrawide Bandgap Solar-Blind UV Photodetectors. *J. Appl. Phys.* **2022**, *131* (15), No. 150901.
(22) Onoda, S.; Hasuike, A.; Nabeshima, Y.; Sasaki, H.; Yajima, K.; Sato, S. -i.; Ohshima, T. Enhanced Charge Collection by Single Ion Strike in AlGaN/GaN HEMTs. *IEEE Trans. Nucl. Sci.* **2013**, *60* (6), 4446−4450.
(23) Tetelbaum, D.; Nikolskaya, A.; Korolev, D.; Mullagaliev, T.; Belov, A.; Trushin, V.; Dudin, Y.; Nezhdanov, A.; Mashin, A.; Mikhaylov, A.; Pechnikov, A.; Scheglov, M.; Nikolaev, V.; Gogova, D. Ion-Beam Modification of Metastable Gallium Oxide Polymorphs. *Mater. Lett.* **2021**, *302*, No. 130346.
(24) Polyakov, A. Y.; Kochkova, A. I.; Azarov, A.; Venkatachalapathy, V.; Miakonkikh, A. V.; Vasilev, A. A.; Chernykh, A. V.; Shchemerov, I. V.; Romanov, A. A.; Kuznetsov, A.; Pearton, S. J. Tuning Electrical Properties in Ga2O3 Polymorphs Induced with Ion Beams. *J. Appl. Phys.* **2023**, *133* (9), No. 095701.
(25) Azarov, A.; Fernández, J. G.; Zhao, J.; He, R.; Park, J.-H.; Jeon, D.-W.; Prytz, Ø.; Djurabekova, F.; Kuznetsov, A. Phase Glides and Self-Organization of Atomically Abrupt Interfaces out of Stochastic Disorder in α-Ga2O3. *Nat. Commun.* **2025**, *16* (1), 3245.
(26) Deák, P.; Duy Ho, Q.; Seemann, F.; Aradi, B.; Lorke, M.; Frauenheim, T. Choosing the Correct Hybrid for Defect Calculations: A Case Study on Intrinsic Carrier Trapping in β-Ga_2O_3. *Phys. Rev. B* **2017**, *95* (7), No. 075208.
(27) Ingebrigtsen, M. E.; Kuznetsov, A. Yu.; Svensson, B. G.; Alfieri, G.; Mihaila, A.; Badstübner, U.; Perron, A.; Vines, L.; Varley, J. B. Impact of Proton Irradiation on Conductivity and Deep Level Defects in β-Ga_2O_3. *APL Mater.* **2019**, *7* (2), No. 022510.
(28) Matsubara, M.; Bellotti, E.; Kyrtsos, A. Migration Mechanisms and Diffusion Barriers of Vacancies in Ga_2O_3. *Phys. Rev. B* **2017**, *95* (24), No. 245202.
(29) Usseinov, A.; Platonenko, A.; Koishybayeva, Z.; Akilbekov, A.; Zdorovets, M.; Popov, A. I. Pair Vacancy Defects in β-Ga2O3 Crystal: Ab Initio Study. *Opt. Mater. X* **2022**, *16*, No. 100200.
(30) Varley, J. B.; Weber, J. R.; Janotti, A.; Van de Walle, C. G. Oxygen Vacancies and Donor Impurities in β-Ga2O3. *Appl. Phys. Lett.* **2010**, *97* (14), No. 142106.
(31) Zacherle, T.; Schmidt, P. C.; Martin, M. Ab Initio Calculations on the Defect Structure of β-Ga_2O_3. *Phys. Rev. B* **2013**, *87* (23), No. 235206.
(32) Onuma, T.; Fujioka, S.; Yamaguchi, T.; Higashiwaki, M.; Sasaki, K.; Masui, T.; Honda, T. Correlation between Blue Luminescence Intensity and Resistivity in β-Ga2O3 Single Crystals. *Appl. Phys. Lett.* **2013**, *103* (4), No. 041910.
(33) Shi, Q.; Wang, Q.; Zhang, D.; Wang, Q.; Li, S.; Wang, W.; Fan, Q.; Zhang, J. Structural, Optical and Photoluminescence Properties of Ga2O3 Thin Films Deposited by Vacuum Thermal Evaporation. *J. Lumin.* **2019**, *206*, 53−58.
(34) Shimamura, K.; Víllora, E. G.; Ujiie, T.; Aoki, K. Excitation and Photoluminescence of Pure and Si-Doped β-Ga2O3 Single Crystals. *Appl. Phys. Lett.* **2008**, *92* (20), No. 201914.
(35) He, X.; Wang, M.; Meng, J.; Hu, J.; Jiang, Y. The Effect of Vacancy Defects on the Electronic Properties of β-Ga2O3. *Comput. Mater. Sci.* **2022**, *215*, No. 111777.
(36) Portoff, A.; Stavola, M.; Fowler, W. B.; Pearton, S. J.; Glaser, E. R. Hydrogen Centers as a Probe of VGa(2) Defects in β-Ga2O3. *Appl. Phys. Lett.* **2023**, *122* (6), No. 062101.
(37) Polyakov, A. Y.; Smirnov, N. B.; Shchemerov, I. V.; Yakimov, E. B.; Yang, J.; Ren, F.; Yang, G.; Kim, J.; Kuramata, A.; Pearton, S. J. Point Defect Induced Degradation of Electrical Properties of Ga_2O_3 by 10 MeV Proton Damage. *Appl. Phys. Lett.* **2018**, *112* (3), No. 032107.
(38) Korhonen, E.; Tuomisto, F.; Gogova, D.; Wagner, G.; Baldini, M.; Galazka, Z.; Schewski, R.; Albrecht, M. Electrical Compensation by Ga Vacancies in Ga_2O_3 Thin Films. *Appl. Phys. Lett.* **2015**, *106* (24), No. 242103.
(39) Chikoidze, E.; Fellous, A.; Perez-Tomas, A.; Sauthier, G.; Tchelidze, T.; Ton-That, C.; Huynh, T. T.; Phillips, M.; Russell, S.; Jennings, M.; Berini, B.; Jomard, F.; Dumont, Y. P-Type β-Gallium Oxide: A New Perspective for Power and Optoelectronic Devices. *Mater. Today Phys.* **2017**, *3*, 118−126.

https://doi.org/10.1021/acs.cgd.5c01728
Cryst. Growth Des. XXXX, XXX, XXX−XXX

(40) Serquen, E.; Bravo, F.; Chi, Z.; Enrique, L. A.; Lizárraga, K.; Sartel, C.; Chikoidze, E.; Guerra, J. A. Impact of C- and m- Sapphire Plane Orientations on the Structural and Electrical Properties of β-Ga2O3 Thin Films Grown by Metal-Organic Chemical Vapor Deposition. *J. Phys. Appl. Phys.* **2024**, *57* (49), No. 495106.
(41) Kaewmeechai, C.; Strand, J.; Shluger, A. L. Structure and Migration Mechanisms of Oxygen Interstitial Defects in β-Ga2O3. *Phys. Status Solidi B* **2026**, *263* (1), No. e202400652.
(42) Binet, L.; Gourier, D. ORIGIN OF THE BLUE LUMINESCENCE OF β-Ga2O3. *J. Phys. Chem. Solids* **1998**, *59* (8), 1241−1249.
(43) Nie, Y.; Jiao, S.; Li, S.; Lu, H.; Liu, S.; Yang, S.; Wang, D.; Gao, S.; Wang, J.; Li, Y. Modulating the Blue and Green Luminescence in the β-Ga2O3 Films. *J. Alloys Compd.* **2022**, *900*, No. 163431.
(44) Onuma, T.; Nakata, Y.; Sasaki, K.; Masui, T.; Yamaguchi, T.; Honda, T.; Kuramata, A.; Yamakoshi, S.; Higashiwaki, M. Modeling and Interpretation of UV and Blue Luminescence Intensity in β-Ga2O3 by Silicon and Nitrogen Doping. *J. Appl. Phys.* **2018**, *124* (7), No. 075103.
(45) Zhu, X.; Zhang, Y.-W.; Zhang, S.-N.; Huo, X.-Q.; Zhang, X.-H.; Li, Z.-Q. Defect Energy Levels in Monoclinic β-Ga2O3. *J. Lumin.* **2022**, *246*, No. 118801.
(46) Frodason, Y. K.; Zimmermann, C.; Verhoeven, E. F.; Weiser, P. M.; Vines, L.; Varley, J. B. Multistability of Isolated and Hydrogenated Ga−O Divacancies in Ga_2O_3. *Phys. Rev. Mater.* **2021**, *5* (2), No. 025402.
(47) Karjalainen, A.; Makkonen, I.; Etula, J.; Goto, K.; Murakami, H.; Kumagai, Y.; Tuomisto, F. Split Ga Vacancies in N-Type and Semi-Insulating β-Ga2O3 Single Crystals. *Appl. Phys. Lett.* **2021**, *118* (7), No. 072104.
(48) Feng, Z.; Bhuiyan, A. F. M. A. U.; Xia, Z.; Moore, W.; Chen, Z.; McGlone, J. F.; Daughton, D. R.; Arehart, A. R.; Ringel, S. A.; Rajan, S.; Zhao, H. Probing Charge Transport and Background Doping in Metal-Organic Chemical Vapor Deposition-Grown (010) β-Ga2O3. *Phys. Status Solidi RRL* **2020**, *14* (8), No. 2000145.
(49) Seryogin, G.; Alema, F.; Valente, N.; Fu, H.; Steinbrunner, E.; Neal, A. T.; Mou, S.; Fine, A.; Osinsky, A. MOCVD Growth of High Purity Ga2O3 Epitaxial Films Using Trimethylgallium Precursor. *Appl. Phys. Lett.* **2020**, *117* (26), No. 262101.
(50) Zhang, Y.; Alema, F.; Mauze, A.; Koksaldi, O. S.; Miller, R.; Osinsky, A.; Speck, J. S. MOCVD Grown Epitaxial β-Ga2O3 Thin Film with an Electron Mobility of 176 Cm2/V s at Room Temperature. *APL Mater.* **2019**, *7* (2), No. 022506.
(51) Alema, F.; Hertog, B.; Ledyaev, O.; Volovik, D.; Thoma, G.; Miller, R.; Osinsky, A.; Mukhopadhyay, P.; Bakhshi, S.; Ali, H.; Schoenfeld, W. V. Solar Blind Photodetector Based on Epitaxial Zinc Doped Ga_2O_3 Thin Film: Solar Blind Photodetector Based on ZnGaO Thin Film. *Phys. Status Solidi A* **2017**, *214* (5), No. 1600688.
(52) Chikoidze, E.; Sartel, C.; Yamano, H.; Chi, Z.; Bouchez, G.; Jomard, F.; Sallet, V.; Guillot, G.; Boukheddaden, K.; Pérez-Tomás, A.; Tchelidze, T.; Dumont, Y. Electrical Properties of P-Type Zn:Ga2O3 Thin Films. *J. Vac. Sci. Technol. A* **2022**, *40* (4), No. 043401.
(53) Alema, F.; Hertog, B.; Osinsky, A.; Mukhopadhyay, P.; Toporkov, M.; Schoenfeld, W. V. Fast Growth Rate of Epitaxial β−Ga2O3 by Close Coupled Showerhead MOCVD. *J. Cryst. Growth* **2017**, *475*, 77−82.
(54) Chi, Z.; Sartel, C.; Zheng, Y.; Modak, S.; Chernyak, L.; Schaefer, C. M.; Padilla, J.; Santiso, J.; Ruzin, A.; Gonçalves, A.-M.; von Bardeleben, J.; Guillot, G.; Dumont, Y.; Pérez-Tomás, A.; Chikoidze, E. Native Defects Association Enabled Room-Temperature p-Type Conductivity in β-Ga2O3. *J. Alloys Compd.* **2023**, *969*, No. 172454.
(55) Nakagomi, S.; Kaneko, S.; Kokubun, Y. Crystal Orientations of β-Ga2O3 Thin Films Formed on m-Plane and r-Plane Sapphire Substrates. *Phys. Status Solidi B* **2015**, *252* (3), 612−620.
(56) Lengyel, K.; Kovács, L.; Péter, Á.; Polgár, K.; Corradi, G. The Effect of Stoichiometry and Mg Doping on the Raman Spectra of LiNbO3:Mg Crystals. *Appl. Phys. B: Laser Opt.* **2007**, *87* (2), 317−322.
(57) Li, Z.; Jiao, T.; Yu, J.; Hu, D.; Lv, Y.; Li, W.; Dong, X.; Zhang, B.; Zhang, Y.; Feng, Z.; Li, G.; Du, G. Single Crystalline β-Ga2O3 Homoepitaxial Films Grown by MOCVD. *Vacuum* **2020**, *178*, No. 109440.
(58) Yao, Y.; Ishikawa, Y.; Sugawara, Y. X-Ray Diffraction and Raman Characterization of β-Ga2O3 Single Crystal Grown by Edge-Defined Film-Fed Growth Method. *J. Appl. Phys.* **2019**, *126* (20), No. 205106.
(59) Dohy, D.; Lucazeau, G.; Revcolevschi, A. Raman Spectra and Valence Force Field of Single-Crystalline β Ga2O3. *J. Solid State Chem.* **1982**, *45* (2), 180−192.
(60) Rao, R.; Rao, A. M.; Xu, B.; Dong, J.; Sharma, S.; Sunkara, M. K. Blueshifted Raman Scattering and Its Correlation with the [110] Growth Direction in Gallium Oxide Nanowires. *J. Appl. Phys.* **2005**, *98* (9), No. 094312.
(61) Janzen, B. M.; Gillen, R.; Galazka, Z.; Maultzsch, J.; Wagner, M. R. First- and Second-Order Raman Spectroscopy of Monoclinic β-Ga_2O_3. *Phys. Rev. Mater.* **2022**, *6* (5), No. 054601.
(62) Zhang, K.; Xu, Z.; Zhao, J.; Wang, H.; Hao, J.; Zhang, S.; Cheng, H.; Dong, B. Temperature-Dependent Raman and Photoluminescence of β-Ga2O3 Doped with Shallow Donors and Deep Acceptors Impurities. *J. Alloys Compd.* **2021**, *881*, No. 160665.
(63) Uchida, T.; Sugie, R. Thermal Stress Analysis in Die-Attached β-Ga2O3 Using Raman Spectroscopy. *Jpn. J. Appl. Phys.* **2023**, *62* (SF), SF1003.
(64) Kranert, C.; Sturm, C.; Schmidt-Grund, R.; Grundmann, M. Raman Tensor Elements of β-Ga2O3. *Sci. Rep.* **2016**, *6* (1), 35964.
(65) Chikoidze, E.; Sartel, C.; Mohamed, H.; Madaci, I.; Tchelidze, T.; Modreanu, M.; Vales-Castro, P.; Rubio, C.; Arnold, C.; Sallet, V.; Dumont, Y.; Perez-Tomas, A. Enhancing the Intrinsic P-Type Conductivity of the Ultra-Wide Bandgap Ga_2O_3 Semiconductor. *J. Mater. Chem. C* **2019**, *7* (33), 10231−10239.

https://doi.org/10.1021/acs.cgd.5c01728
Cryst. Growth Des. XXXX, XXX, XXX−XXX